

Floating light-activated microelectrical stimulators tested in the rat spinal cord

This article has been downloaded from IOPscience. Please scroll down to see the full text article.

2011 J. Neural Eng. 8 056012

(<http://iopscience.iop.org/1741-2552/8/5/056012>)

View [the table of contents for this issue](#), or go to the [journal homepage](#) for more

Download details:

IP Address: 128.197.177.205

The article was downloaded on 14/09/2011 at 17:32

Please note that [terms and conditions apply](#).

Floating light-activated microelectrical stimulators tested in the rat spinal cord

Ammar Abdo¹, Mesut Sahin^{1,4}, David S Freedman², Elif Cevik³,
Philipp S Spuhler³ and M Selim Unlu^{2,3}

¹ Biomedical Engineering Department, New Jersey Institute of Technology, NJ, USA

² Electrical and Computer Engineering, Boston University, MA, USA

³ Biomedical Engineering, Boston University, MA, USA

E-mail: sahin@njit.edu

Received 30 June 2011

Accepted for publication 23 August 2011

Published 14 September 2011

Online at stacks.iop.org/JNE/8/056012

Abstract

Microelectrodes of neural stimulation utilize fine wires for electrical connections to driving electronics. Breakage of these wires and the neural tissue response due to their tethering forces are major problems encountered with long-term implantation of microelectrodes. The lifetime of an implant for neural stimulation can be substantially improved if the wire interconnects are eliminated. Thus, we proposed a floating light-activated microelectrical stimulator (FLAMES) for wireless neural stimulation. In this paradigm, a laser beam at near infrared (NIR) wavelengths will be used as a means of energy transfer to the device. In this study, microstimulators of various sizes were fabricated, with two cascaded GaAs p-i-n photodiodes, and tested in the rat spinal cord. A train of NIR pulses (0.2 ms, 50 Hz) was sent through the tissue to wirelessly activate the devices and generate the stimulus current. The forces elicited by intraspinal stimulation were measured from the ipsilateral forelimb with a force transducer. The largest forces were around 1.08 N, a significant level of force for the rat forelimb motor function. These *in vivo* tests suggest that the FLAMES can be used for intraspinal microstimulation even for the deepest implant locations in the rat spinal cord. The power required to generate a threshold arm movement was investigated as the laser source was moved away from the microstimulator. The results indicate that the photon density does not decrease substantially for horizontal displacements of the source that are in the same order as the beam radius. This gives confidence that the stimulation threshold may not be very sensitive to small displacement of the spinal cord relative to the spine-mounted optical power source.

(Some figures in this article are in colour only in the electronic version)

1. Introduction

Electro-magnetic, optical or acoustic energy can be wirelessly transferred to neural tissue to stimulate the neurons remotely [1, 2] or modulate their activity [3]. These direct methods of wireless neural stimulation are not yet commonplace in neural prosthetic applications due to the high levels of energy needed and the bulky extracorporeal equipment required. One way to reduce energy requirements is to use an implantable microstimulator that can harvest the energy first and then deliver it to the local tissue whenever the stimulation is

needed. Energy storage and pulse shaping can also be achieved through electronics that can be incorporated into this wireless device. However, any additional component that can increase the device size should be avoided for microstimulation applications in the CNS because of concerns with tissue trauma. A completely passive device that harvests the energy and instantaneously converts it to electric pulses for stimulation would also reduce the risk of failure because of its simplicity of operation.

Our group has been investigating a floating light-activated microelectrical stimulator (FLAMES) that contains passive photodiodes for wireless activation of neural tissue using near

⁴ Author to whom any correspondence should be addressed.

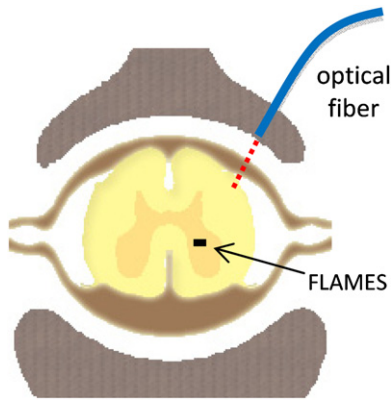


Figure 1. Envisioned implantation paradigm for chronic microstimulation of the spinal cord gray matter using a FLAMES and an optical fiber that delivers the stimulation energy in the form of NIR light through the neural tissue.

infrared (NIR) light for energy transmission [4, 5]. In the envisioned paradigm, the microstimulator is implanted into the neural tissue at the targeted site in the CNS, e.g. the spinal cord gray matter, typically a few millimeters below the pial surface. The laser pulses are sent through a multi-mode optical fiber placed near the microstimulator to activate it. The tip of the optical fiber is inserted through a hole into the vertebrae just above the microstimulator, but located outside the dura matter (figure 1). Therefore, the distance that the laser beam has to travel is of the order of a few millimeters through the neural tissue before reaching the microstimulator. The laser source and control electronics are implanted at a distant site, e.g. the subclavicular area, that is most convenient for transcutaneous charging of batteries and programming of the pulse parameters using RF telemetry.

Wireless stimulators have been reported by other groups [6–8]; an optically activated, yet tethered, microstimulator was shown to stimulate the rat sciatic nerve [6]. This design apparently does not intend to address the problems of interconnects since it is attached to a fiber-optic tail that replaces the wires. Optical energy is delivered via the optical fiber rather than being transmitted through the neural tissue, as with the current design. An ultrasonically powered wireless device was also proposed for nerve stimulation [7]. The stimulator length is 8 mm in a recently reported version and thus may be too large for CNS applications. BION™ stimulator is an example of a wireless stimulator that is controlled by radio-frequency electromagnetic waves and designed to be used in the peripheral nervous system [8]. Because the telemetry and power circuitry are incorporated into the stimulator, the device size is of the order of centimeters.

The main objective of this study was to investigate the feasibility of the FLAMES approach for intraspinal microstimulation (ISMS), which has been investigated as a potential technique for recovering function in a number of conditions caused by spinal cord injury (SCI). The spinal cord includes specialized neural circuits that can autonomously generate coordinated muscle activity [9]. It was shown that

a few electrodes implanted in the cat spinal cord within the lumbosacral region can produce locomotion [10–12]. Losing somatic and visceral functions, such as limb movements and bladder voiding, are some of the disabilities that result from SCI. The feasibility of ISMS for limb and bladder control has been demonstrated in animal models [13]. Breakage of interconnects [14] and chronic tissue response induced by the micromotion of electrodes [15] is a major impediment before ISMS can be pilot studied in human subjects [16]. Electrodes made with flexible wires have been demonstrated to last for several years in the cortex [17, 18]. However, the interconnect longevity in the feline spinal cord is rarely more than a year [19]. In an attempt to test the feasibility of ISMS for bladder control in cats, ~20% of the electrodes implanted in the sacral spinal cord became non-functional due to lead failures after three months of implantation [19]. In another study where the cat lumbar region was microstimulated to generate leg movements, only 67% of the electrodes remained functional after six months of implantation [20].

The human spinal cord experiences substantial translational and rotational displacements that make chronic implantation of microwire electrodes very challenging. For instance, the log-roll rehabilitation technique developed for traumatic SCI subjects generated $7.3 \pm 5.8^\circ$ of flexion/extension and $7.9 \pm 9.1^\circ$ of axial rotation of the cervical cord, as tested in cadavers [21]. A floating, wireless microstimulator can be an important step toward the development of such a system for use in human subjects.

Single-channel wireless stimulators may resolve or alleviate these problems by eliminating the tethering forces due to interconnects, which is the primary source of chronic tissue reaction [22]. With no wires attached, the implanted device would float and move together with the surrounding neural tissue as it goes through deformations, with translational and rotational displacements thereby substantially reducing the shear forces at the device–tissue interface.

Various sizes of FLAMES were fabricated in the submillimeter range with integrated gallium arsenide (GaAs) p-i-n photodiodes. The current–voltage (I – V) curves were obtained to show the photodiode characteristics of the devices. The gold contacts were coated with poly 3,4-ethylenedioxythiophene (PEDOT) to improve the charge injection capacity (CIC). The devices were placed in a saline solution to measure the stimulation voltage near the cathode in a conductive medium. The FLAMES were then tested in the rat cervical spinal cord for activation of forelimb musculature. The forces generated through ISMS were measured from the ipsilateral forelimb with a force transducer.

2. Methods

2.1. Device fabrication

The III–V semiconductor heterojunction structure in figure 2(A) was designed and then grown at the Institute of Electronic Materials Technology, Poland on a GaAs substrate. The tandem device was designed to have two p-i-n photodiodes connected through a highly doped tunneling junction. The

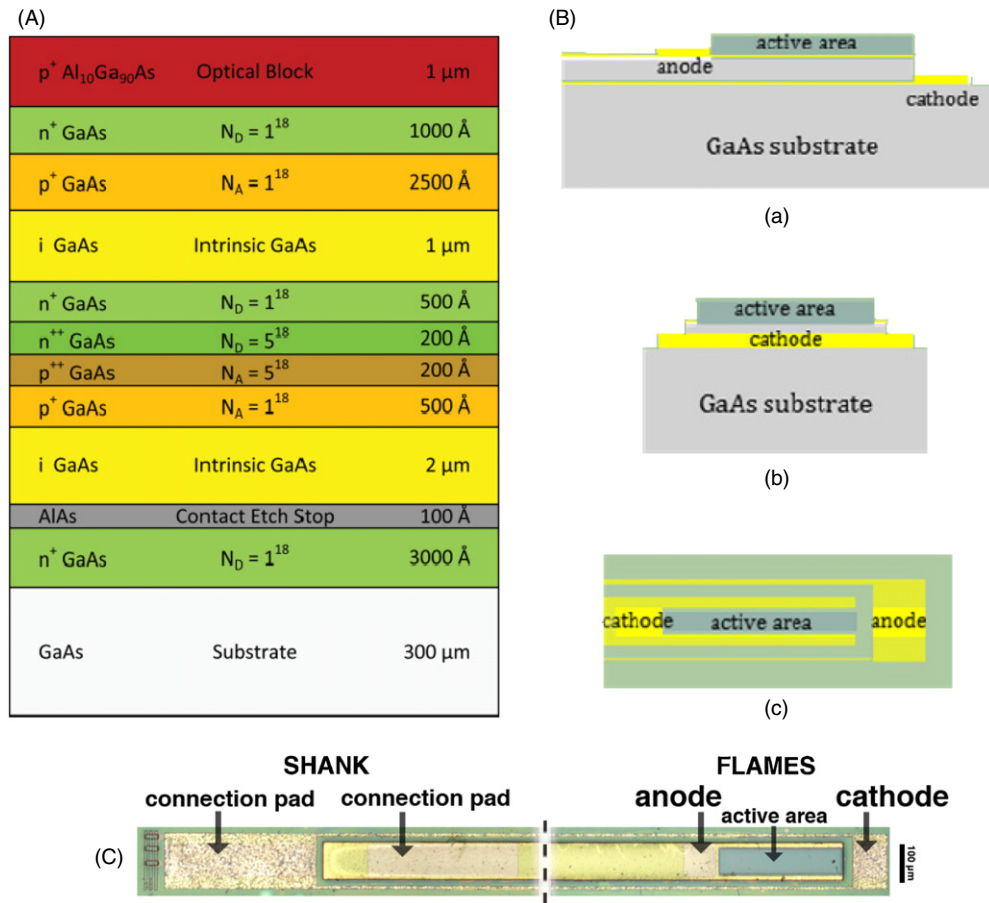


Figure 2. (A) $Al_xGa_{(1-x)}As$ heterojunction structure used in the fabrication of the FLAMES devices. (B) (a) side view, (b) front view and (c) top view of FLAMES device after etching and thin film depositions. (C) Annotated micrograph of a type C device showing the layout at the tip of a 3.5 mm shank (an extension of the substrate for handling the device during testing). The scale bar is 100 μm .

top part of the device, the optical blocking layer, contains a one-micron thick film of $Al_{10}Ga_{90}As$ to absorb the unwanted lower wavelengths and prevent them from reaching the photodiodes.

Aluminum gallium arsenide/gallium arsenide ($AlGaAs/GaAs$) FLAMES were fabricated in different sizes. Die pieces of $1 \times 1 \text{ cm}^2$ were diced from the custom $AlGaAs/GaAs$ 50.4 mm wafer. S1813 positive photoresist (Shipley, MA) was used to pattern the devices for all steps. Mesa etching was utilized to micromachine the custom wafer in figure 2(A) into the vertical structure shown in figure 2(B). Selective wet etching was used to reach the doped n-layer by utilizing AlAs etch stop. Wet etchant for etching to p-type layer was a 25:5:1 deionized (DI) H_2O /phosphoric acid/ H_2O_2 solution. The p metal layer was deposited with Pt: Ti: Pt: Au : 100: 400: 100: 1500 \AA and annealed at 400 $^\circ C$ for 1 min. For etching to n-type layer, a selective etchant was prepared by mixing 5.5 ml H_2O_2 and 50 ml citric acid solution (1 g citric acid dissolved in 2 g DI H_2O) to etch GaAs and $Al_xGa_{1-x}As$ layers and stop at the AlAs etch stop. It is very important to remove the thin surface oxide layer of the cap layer before etching. This was achieved by dipping the device in 15:1 DI H_2O /buffered oxide etch

(BOE) solution for 10 s. Then, a short dip in 15:1 H_2O /BOE removed the AlAs layer. The n metal deposition consisted of Ge: Au: Ge: Au: Ni: Au (60: 100: 100: 240: 100 : 1500 \AA) layers, which was then annealed at 430 $^\circ C$ for 1 min. A 300 nm silicon nitride layer was deposited with PECVD and patterned. The top silicon nitride layer was then etched with CF_4 plasma. The devices were released using a rotary dicing saw and a backside etch to thin the devices until they were approximately 100–150 μm thick. Finally, the devices were cleaned using a dilute hydrofluoric acid bath and a long plasma oxygen descum. A micrograph of a fabricated device is shown in figure 2(C).

2.2. Probe station measurements

Fabricated devices were optically characterized using a focused output from a multimode fiber that was imaged on the active area of the p-i-n photodiode. The device was placed on a mechanical stage that was adjusted to ensure that the optical beam was contained within the active area. BeCu coated tungsten probe tips (T-4 125-BeCu, GGB Industries, FL) were affixed to three-axis micromanipulators and connected to a semiconductor parameter analyzer (HP 4156A) where low frequency $I-V$ measurements were performed. The devices

were tested under two different optical powers, 0 and 30 μW with an 856 nm wavelength laser diode.

Two photodiodes were vertically connected in series to increase the output voltage. The long metal connections on the shank devices were not insulated from the semiconductor material, creating a resistive path for carriers. This resulted in a lower turn-on voltage than expected for two photocells in series. Non-shank devices did not exhibit this reduction in voltage, but the shanks were necessary for securing the devices to a micromanipulator during *in vivo* testing. The optical blocking layer on top reduces the efficiency of our devices. This layer was originally included in the design to test the idea of wavelength selectivity, but not further investigated in this report. Thus, our series photodiodes exhibit a relatively modest conversion efficiency of 11% (in agreement with simulations), which should typically be above 40% without the blocking layer [6].

2.3. Volume conductor measurements

PEDOT was deposited on the gold stimulation contacts using electrochemical polymerization with 10 mM of PSS in an EDOT solution at 1.5 mA cm^{-2} and allowing sufficient time for the contacts to turn black [23]. Overcoating was avoided to prevent flaking off the PEDOT film. The stimulator was secured at the bottom of a petri dish filled with normal saline (0.9%) solution diluted ten times to simulate neural tissue impedance ($\sim 600 \Omega\text{cm}$). A tungsten microelectrode was placed immediately above the cathode ($\sim 10\text{--}30 \mu\text{m}$), without making direct contact, to record the voltage field generated by the FLAMES. A high input-impedance buffer amplifier (TLC2274, Texas Instruments) was utilized in this part and a large Ag/AgCl electrode as a reference. The stimulation voltage was measured in response to a single laser pulse at 830 nm (PW = 0.2 ms). The laser source (DLS-500-830FS-100, StockerYale, Canada, 74 mW) and acquisition of signals into a computer was controlled through MATLAB (MathWorks). The laser power was varied from zero to maximum to study the voltage field near the contacts in the medium.

2.4. *In vivo* testing

In six Sprague–Dawley rats (350–500 g), anesthesia was induced with intraperitoneal injection of ketamine (80 mg kg^{-1}) and xylazine (12 mg kg^{-1}) mixture diluted with saline. Further doses of ketamine were administered to maintain the anesthesia as needed. Marcaine (0.2 mL) was injected at the site of incision as a local anesthetic. The rectal temperature was continuously monitored and maintained between 36 and 37 $^{\circ}\text{C}$ using a temperature regulated heating pad. The head was stabilized in a stereotaxic frame and the spinal cord was immobilized from the spinous process at T1. Laminectomy was performed at C5–C7 and the dura was removed. The spinal cord was kept moist using warm saline. All procedures were approved and performed in accordance with the guidelines of the Animal Care and Use Committee, Rutgers University, Newark, NJ.

Three different device sizes with a top layout as shown in figure 2(C) were tested in this study. The largest device, type

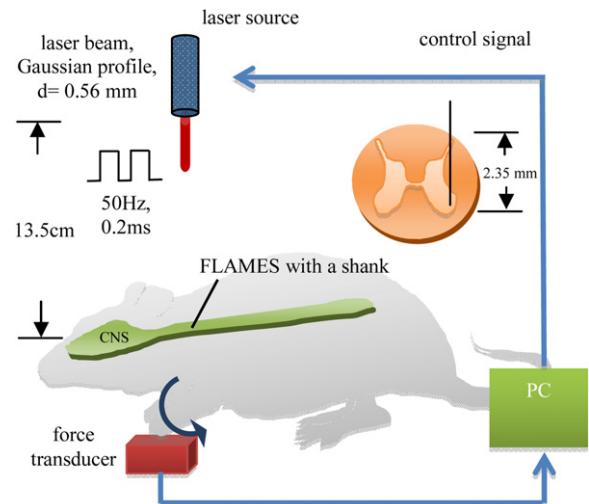


Figure 3. Intraspinal cord microstimulation setup for *in vivo* testing of FLAMES in rats. The FLAMES is located at the tip of a shank that is inserted into the cervical spinal segment C6. The instantaneous power and the pulse width of the laser pulses are controlled via the computer. The forelimb extension forces generated by the ISMS are recorded by a force transducer attached to the ipsilateral hand.

A, had cathodic and anodic areas of 11 500 μm^2 each, an active area of 28 500 μm^2 , and a total device size of 200 \times 700 μm^2 . These values for type B and C devices were 8 500 and 5 500 μm^2 , 25 500 and 17 500 μm^2 , and 170 \times 600 and 140 \times 500 μm^2 , respectively. Figure 3 shows the preparation used for intraspinal stimulation in anesthetized animals. The FLAMES was inserted into the cervical spinal cord at an angle of 30 $^{\circ}$ (from the normal) near the left or right dorsal root entry zone and reaching the ventral horn on the ipsilateral side using a three-axis micromanipulator (inset). The laser was placed 13.5 cm above the cord using another micromanipulator and the built-in lenses were adjusted to form a beam with a circular footprint of 0.56 mm in diameter at the cord surface aiming at the photodiode from above. A train of NIR pulses (0.2 ms pulse width, 50 Hz, 500 ms duration) was sent to the device through the tissue. The power of the laser source was gradually increased until twitches in the forelimb were observed. The power at that level was considered the threshold (P_{th}). Then, the laser power was increased incrementally while the forces generated via spinal cord stimulation were measured with a transducer attached to the ipsilateral hand. The photodiode currents at threshold power were also measured at various depths from all devices (A, B and C) using a current amplifier, which short-circuited the device output to zero volts (hence no stimulation), preventing the current flow through the internal diode.

The laser beam used in this study had a Gaussian profile with a circular footprint. The radius was taken at $\sqrt{2}\sigma$ of the Gaussian profile, which is the distance where the intensity drops down to $1/e^2$ of its peak in 2D plane. This diameter corresponds to the diameter of a flat profile circular beam with the same peak power density and the same total power as the Gaussian profile laser. The instantaneous power was

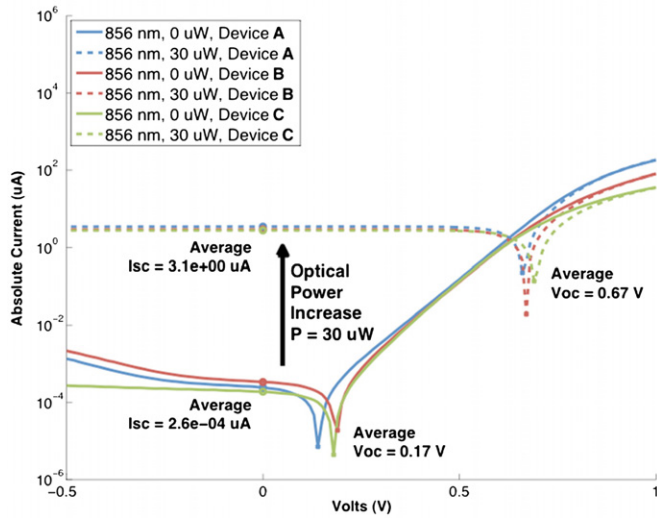


Figure 4. *I-V* measurements obtained using a bench top optical probe station.

controllable and varied linearly with the control signal, as specified by the manufacturer. The incident power density at the cord surface (in mW cm^{-2}) was calculated accordingly for a train of pulses using the following equation:

$$\text{power_density} = \frac{P}{A} \times \text{PW} \times f, \quad (1)$$

where P is the peak power of the laser pulse controlled by the computer (mW); A is the cross-sectional area of an equivalent, uniform profile beam at the cord surface (cm^2); PW is the pulse width (s) and f is the frequency (Hz).

3. Results

3.1. Bench top measurements

Devices were tested using 856 nm excitation from a laser diode. Figure 4 shows the measured *I-V* characteristics for the three devices with and without illumination. All three devices have similar open circuit voltages (V_{OC}) and short circuit currents (I_{SC}). When used as a stimulator, the device operates in the photovoltaic mode. That is, depending on the load resistance, the device will operate between the short-circuit current and open-circuit voltage. There was no evidence of breakdown for a reverse bias of 30 V. Responsivity was about 0.1 A W^{-1} for all devices.

3.2. Volume conductor measurements

The voltage field recorded immediately above the cathode in saline is shown in figure 5(A) for device C. The peak voltage $\sim 30 \mu\text{m}$ above the cathodic contact was around 110 mV and stayed flat for the duration of 0.2 ms pulse. This suggests that the contact-medium interface has a sufficiently large CIC to maintain a constant current. The test was conducted at various frequencies within a range of 10–100 Hz. The peak voltage was stable and the interface was discharged completely during the OFF cycles through the leakage currents of the photodiodes [24]. Figure 5(B) shows the voltage field in saline immediately

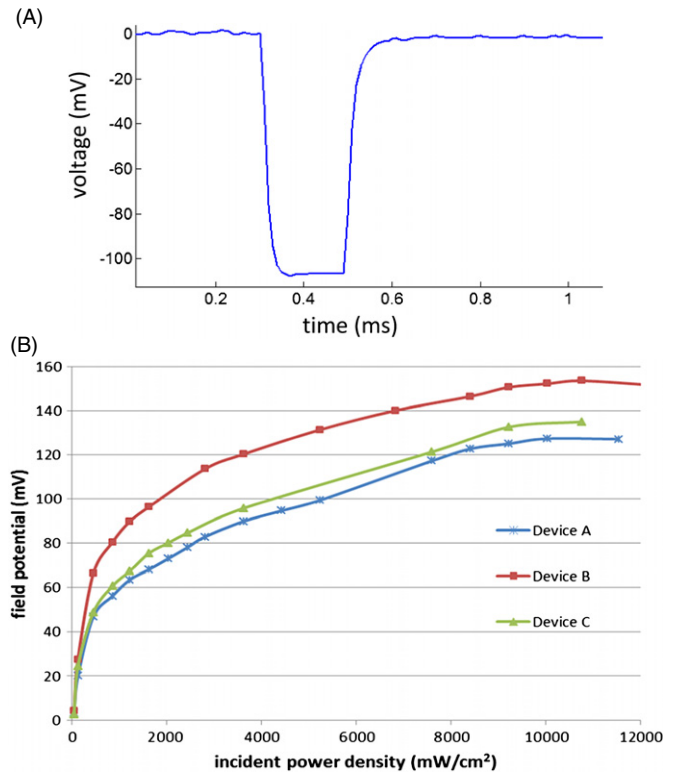


Figure 5. Volume conductor measurements. (A) Waveform recorded $\sim 30 \mu\text{m}$ above the center of the cathode (of device C) as a response to a single laser pulse. (B) Field potential recorded immediately ($\sim 10 \mu\text{m}$) above the cathodes with respect to an Ag/AgCl electrode of devices A, B and C as a function of incident light power. Note that this is the instantaneous incident power density (not multiplied by the duty cycle, which is $\text{PW} \times f = 1\%$) at the surface of the volume conductor.

above the cathode of devices A, B and C as a function of laser power. The voltage exponentially increases and then plateaus at a laser power where the internal pn junctions start limiting the device voltage. The voltage pulse amplitude was very sensitive to the electrode tip distance from the contact. Vibrations of the tungsten recording electrode induced some variations into the plots.

3.3. In vivo testing

Elbow extension was the type of movement typically generated in C6 by stimulating the most ventral locations in the cord. The device tip and thus the cathodic contact was inserted about 2.35 mm below the dorsal pial surface to generate this forelimb movement. Figure 6(A) shows the reproducibility of the vertical component of the force generated during a 0.5 s ON- 1.5 s OFF cycle for 15 s in one of the animals. The force in each cycle is fused and stable at 50 Hz train frequency without any signs of fatigue (figure 6(B)). As control, the muscle contractions were completely blocked everytime an opaque object was placed in the path of NIR light.

The forelimb extension forces are plotted in figure 7 collectively from all experiments as a function of incident laser power density at the cord surface. The largest forces produced with devices A, B and C were around 0.82, 0.8 and 1.08 N respectively. The smallest and largest stimulation

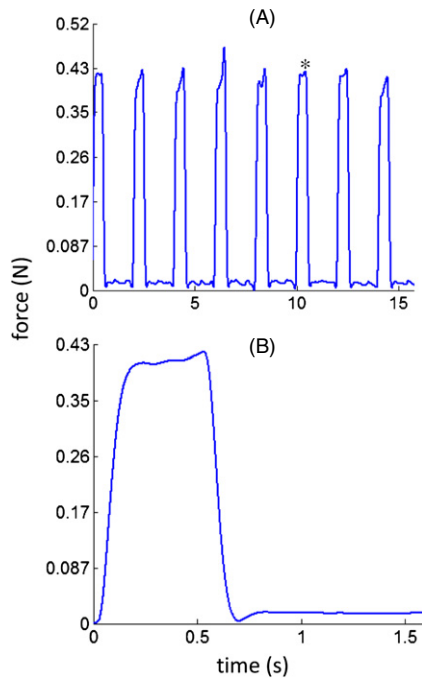


Figure 6. Vertical component of the elbow extension force recorded with a transducer attached to the ipsilateral hand in rat 3: (A) for a series of 0.5 s ON- 1.5 s OFF cycles. Each tetanic force is generated by a train of 50 Hz, 0.2 ms pulses. (B) Sample cycle expanded from the plot in A (marked with *) to demonstrate tetanus.

current values injected into the tissue were around 6 ± 2.5 and $120 \mu\text{A}$ for all devices, respectively. The variations in the plots are due to slightly different implant locations in each animal.

Force measurements are clustered into two groups. One group is in a low-threshold area and the other is in a high-threshold area. The two areas show two distinct behaviors. The low-threshold area has a larger slope where the force reaches the threshold at relatively small laser powers but elicits larger forces. The high-threshold area has a smaller slope where in some cases nine-times higher power was required to reach half the force generated in the low-threshold area (e.g. rat 4: device B versus rat 5: device A). In rat 4, data from both areas were obtained for comparison. The electrodes were moved a few hundred micrometers up to repeat the experiment into the high threshold area. In rat 5, the low-threshold area behavior was also seen but the device tip had to be moved a few hundred micrometers above to avoid fatigue.

An example strength duration curve, which we define as the threshold laser power as a function of pulse width, is shown in figure 8 from one of the trials (dashed line). The microstimulator was located in the low-threshold region in the cord, as identified in figure 7. Threshold power decreases exponentially by the pulse width as expected in a strength-duration curve. Only a few milliwatts suffice for activation with pulses longer than 0.2 ms. The solid line in the figure is the curve fit generated using Lapicque's equation for strength-duration curve on intracellular stimulation of neurons [25]. The chronaxie time and rheobase power are found as 0.27 ms and 1.5 mW, respectively, from the experimental data, which agrees well with the theoretical curve fit.

The threshold power was investigated as the laser source was moved away along the spinal cord (figure 9). The vertical axis is in multiples of the threshold power that was measured when the beam was aligned with the active area of the microstimulator (P_{th}). The threshold power had to be increased 1.15 ± 0.12 times when the source moved $250 \mu\text{m}$ away from the center. Similarly, a 4 ± 0.37 times higher power was required to produce the threshold arm movement when the source was displaced by 1 mm.

4. Discussion

4.1. NIR exposure limitation

The NIR exposure safety limit is given only for the skin and retina by American National Standards for Safe Use of Lasers (ANSI Z136.1-2007). Radiating the neural tissue with light can cause temperature elevation that can be harmful to the tissue if the temperature increases by more than 1°C [26]. Computer simulations suggested that in order to keep temperature elevation under 0.5°C in the neural tissue, NIR exposure needs to be limited to 325 and 250 mW cm^{-2} for gray and white matter, respectively [27]. The maximum incident power density used in this study was 75 mW cm^{-2} , which is only a fraction of our predicted maximum allowable exposure.

Optical properties of tissue determine the penetration depth of light. The scattering coefficient is the most important factor that determines the number of photons available at any given depth. It is important to note that the scattering coefficient values reported in the literature for human and animal neural tissues vary within a large range [28–30]. The human spinal cord is also about two-and-a-half times thicker (sagittally) than the rat spinal cord at the cervical level (5.8 mm at C6) [31]. ISMS of human spinal cord may be more demanding because the targeted sites for stimulation may be deeper in the cord. Considering all these species differences, simulations suggested that microstimulation of human spinal cord is feasible using comparable sizes of FLAMES to those in this study [27].

The microstimulators were efficient enough to convert the relatively small amount of NIR light available at a depth of 2.35 mm inside the neural tissue to a sufficient electrical current for ISMS. This suggests multiple FLAMES can be activated next to each other without exceeding the safe level of NIR exposure. On the other hand, it should be mentioned that in chronic applications the amount of current required for stimulation is higher due to encapsulation of electrodes with connective tissue. This warrants further testing of FLAMES with long-term implants.

In the envisioned chronic stimulation paradigm (figure 1), the laser source will be fixed to the vertebral bone and therefore the devices may move in and out of focus as the spinal cord is moving inside the vertebrae. The experimental setup did not allow us to test for changes in the threshold power for rotational displacements. The longitudinal translations of the source suggested that the threshold increases by four times for a displacement of about four times the laser beam radius. Increasing the beam size can also reduce the sensitivity to source displacement. As a trade off, however, a larger tissue volume would be radiated by the laser beam.

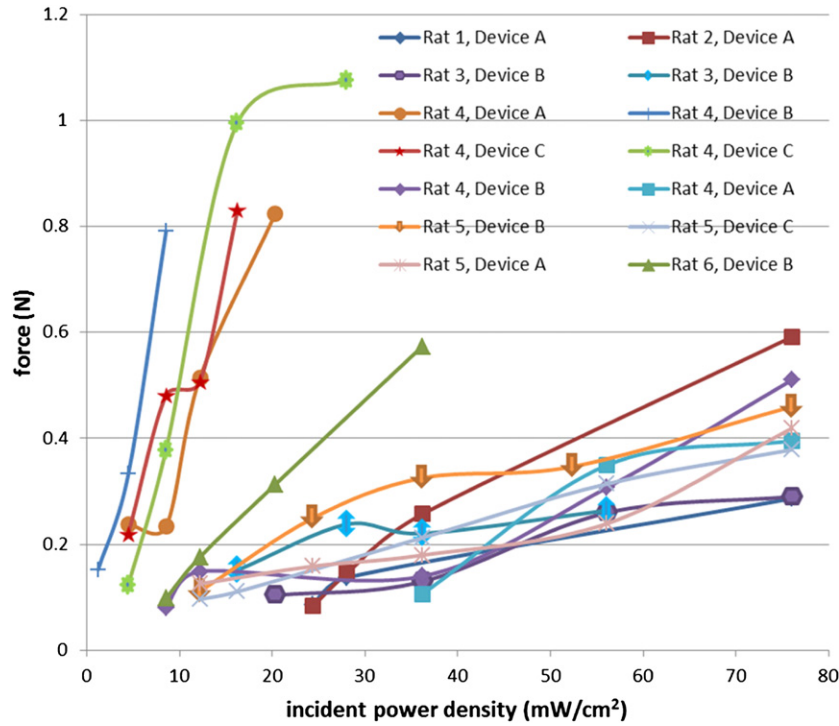


Figure 7. Forelimb extension forces generated by ISMS at 50 Hz ($PW = 0.2$ ms) as a function of incident laser power density calculated at the spinal cord surface according to equation (1).

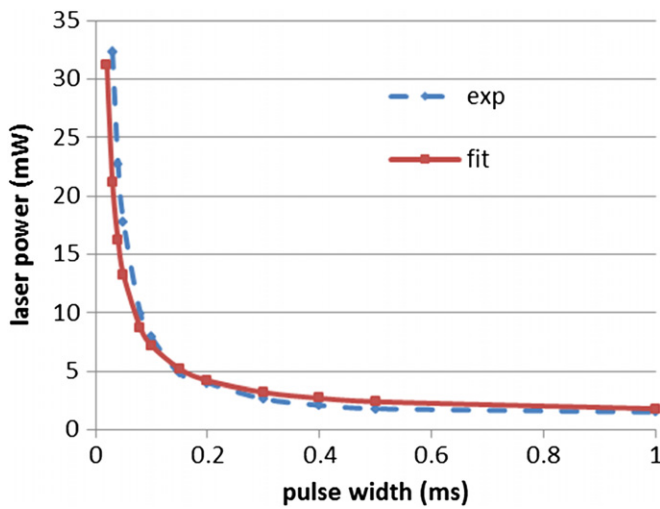


Figure 8. Strength–duration curve results obtained with device C in rat 4 (dashed line). The solid line is the curve fit using Lapicque’s strength–duration equation. The pulse width was varied from $30 \mu s$ to 1 ms while searching for the threshold laser power needed to generate smallest arm twitches.

4.2. Microstimulator sizes

Three different-sized devices were tested in this study. One of the goals of this research is to minimize the device size while generating sufficient current for stimulation. Minimizing the stimulator size is crucial in order to reduce the neural tissue replaced by the implant and the long-term immunological response. Depending on the desired volume of tissue to be stimulated, the device dimensions can be further reduced. Computer simulations indicated that the maximum device

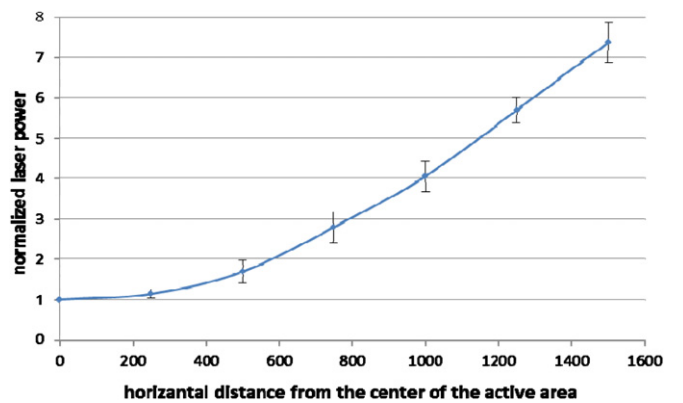


Figure 9. Threshold laser power shown in multiples of P_{th} as a function of the laser source displacement from the center of the device active area. The devices were implanted at ~ 2.35 mm below the pial surface. Data represent the average of eight trials from four rats using all three types of device in most animals.

output voltage, or the number of photodiodes in series, can also be used as a free parameter in order to minimize the device dimensions [27].

4.3. Contact material

Injection of high currents through micro-size contacts imposes a challenge for the electrode–electrolyte interface. The voltage across the interface is limited by the water window whether the current is injected through faradic or capacitive mechanisms. Several materials have been investigated for their high CIC. Iridium oxide (IrOx) contacts obtained either by activation of iridium or sputtering process can achieve a large CIC by anodically biasing the electrode [32]. However,

Table 1. Comparison of stimulus parameters with other studies.

Current (μA)	Freq. (Hz)	PW (ms)	Spinal cord section	Preparation	Ref.
6–120 μA	50	0.2	Rat ventral horn in C6	Anesthetized/intact	This study
32 ± 19 , $1-4 \times$ threshold	40–50	0.2	Cat lumbosacral cord (multiple regions)	Decerebrated/spinalized	[11]
<100	300	0.25–0.3	Cat lumbar cord (multiple regions)	Anesthetized/spinalized	[42]
1–15	75	0.3	Interneuronal region in rat lumbar cord	Decerebrated/spinalized	[43]
50–100	40	0.1	Cat lumbar spinal cord (multiple regions)	Decerebrated/intact spinal cord	[35]

anodic biasing requires additional active circuitry on the device. Therefore, materials that can provide high CIC at the open circuit voltage of the interface may be a better choice for passive microstimulators. Some electrode materials that use capacitive mechanism are tantalum oxide (TaOx), titanium nitride (TiN) and poly (3,4-ethylenedioxythiophene) (PEDOT). In this study, the charge capacity utilized from the contacts was calculated as $436 \mu\text{C cm}^{-2}$ (i.e. $120 \mu\text{A} \times 0.2 \text{ ms}/500 \mu\text{m}^2$), which is well below the CIC reported for PEDOT (2.3 mC cm^{-2}) [33]. This indicates that contacts could be made smaller without exceeding the CIC of the electrode–electrolyte interface. This would leave a larger top surface area for the photodiodes and in turn increase the output current. Thus, the CIC of the contact material directly affects the stimulator output, which can be traded for a smaller device size if necessary [27].

4.4. Animal model and the site of stimulation

Rats and cats have been used as animal models for ISMS. Anatomical differences are present between the two models; however, rat is advocated as a better model for its similarity of upper limb biomechanics to humans [34]. In this study, the forelimb forces were stable and reproducible within each implant. The point of stimulation was ‘easy’ to find in all trials.

Elbow extension was obtained by stimulating the C6 segment at the ventral horn. Various groups have reported that microstimulation of the ventral sites generates extension and the sites that produce flexion are located more dorsally in the cat [35]. Our investigation located a low-threshold area near the C6 ventral horn for generation of elbow extension in the rat spinal cord. Small forces were also observed while stimulating the intermediate and dorsal regions at C5–C7 (data not shown). ISMS was applied in monkey cervical region to induce forelimb movements [36]. Elbow extension was generated by stimulating C6–C8 segments.

ISMS of the ventral horn can activate various neuronal compartments, such as motor neurons, interneurons, specific synaptic inputs from different regions and afferents [37]. Therefore, it is not possible to determine the exact element(s) being stimulated. The site of stimulation was not marked in this study because FLAMES did not include microfluidic channels, nor was it possible to pass dc current without damaging contacts. Therefore, we can only estimate the site of stimulation from the depth of penetration. In the low-threshold area, we suspect that the cathodic contact was located near the alpha motor neuron axons on the ventral side where they

bundle before exiting the cord. Axons have lower threshold than soma when cathodic stimulation is used, as reported in several studies [38–40]. The force increased as the power increased monotonically in all graphs. The relation between the force and incident power density looks different in each rat, which is possibly due to slightly different implant locations in the spinal cord. Inter-animal neuroanatomical differences may have contributed to the variations in the plots as well.

The largest force recorded in all experiments was 1.08 N and the average of the largest forces from 14 trials was 0.53 N. This level of force produced from a rat forelimb is functional considering the body weight of the animals (350–500 g). John Stanford *et al* reported a maximum force of 0.46 N from rats as they extended their forelimb through a rectangular slot to press on a lever [41].

The threshold current amplitudes needed to stimulate the ventral horn were about $6 \pm 2.5 \mu\text{A}$ (mean \pm std, in low-threshold area) and the largest current used in the high-threshold area was about $120 \mu\text{A}$; these are comparable to values reported by other groups (table 1) that have investigated the feasibility of ISMS to restore locomotion. We did not find a low-threshold area in the interneuronal region, as reported by others (34), in the rat cervical spinal cord (C5–C7) under ketamine/xylazine anesthesia.

5. Conclusions

Prototype floating microstimulators were fabricated in a vertical heterojunction structure on a GaAs substrate. Attempts were made to maximize stimulation efficiency by increasing the output voltage with cascaded photodiodes, coating the contacts with a high CIC material, and locating a low-threshold area in the rat spinal cord. The forces generated and *in vitro* voltage measurements support the premise that submillimeter-size optically activated microstimulators can generate sufficient currents of functional value. Microstimulation of the human spinal cord is predicted to demand higher levels of NIR illumination. The fact that very low levels of laser power could generate functional limb forces in rats is encouraging for translation of this method to the human spinal cord.

Acknowledgment

This study was funded by National Institute of Health/NINDS (R21 NS050757) and NIBIB (R01 EB009100).

References

- [1] Hsu K H et al 2003 Analysis of efficiency of magnetic stimulation *IEEE Trans. Biomed. Eng.* **50** 1276–85
- [2] Wells J et al 2005 Optical stimulation of neural tissue *in vivo* *Opt. Lett.* **30** 504–6
- [3] Yoo S S et al 2011 Focused ultrasound modulates region-specific brain activity *NeuroImage* **56** 1267–75
- [4] Sahin M and Ur-Rahman S S 2007 Finite element analysis of a floating microstimulator *IEEE Trans. Neural Syst. Rehabil. Eng.* **15** 227–34
- [5] Gray K M et al 2003 Voltage field generated by a single photodiode in a volume conductor: simulation and measurements *Proc. 25th Annu. Int. Conf. of IEEE/EMBS (Cancun, Mexico, 2003)* **3** pp 2189–92
- [6] Song Y K et al 2007 A microscale photovoltaic neurostimulator for fiber optic delivery of functional electrical stimulation *J. Neural Eng.* **4** 213–8
- [7] Larson P J and Towe B C 2011 Miniature ultrasonically powered wireless nerve cuff stimulator *5th International IEEE/EMBS Conf. on Neural Engineering, NER 2011 (Cancun, Mexico, 2011)* pp 265–8
- [8] Loeb G E et al 2001 BION™ system for distributed neural prosthetic interfaces *Med. Eng. Phys.* **23** 9–18
- [9] Sherrington C S 1910 Flexion-reflex of the limb, crossed extension-reflex and reflex stepping and standing *J. Physiol.* **40** 28–121
- [10] Mushahwar V K et al 2002 Intraspinal microstimulation generates locomotor-like and feedback-controlled movements *IEEE Trans. Neural Syst. Rehabil. Eng.* **10** 68–81
- [11] Saigal R et al 2004 Intraspinal microstimulation generates functional movements after spinal-cord injury *IEEE Trans. Neural Syst. Rehabil. Eng.* **12** 430–40
- [12] Tai C et al 2003 Multi-joint movement of the cat hindlimb evoked by microstimulation of the lumbosacral spinal cord *Exp. Neurol.* **183** 620–7
- [13] Pikov V 2008 Clinical applications of intraspinal microstimulation *IEEE* **96** 1120–8
- [14] Hetke J F et al 1994 Silicon ribbon cables for chronically implantable microelectrode arrays *IEEE Trans. Biomed. Eng.* **41** 314–21
- [15] McConnell G C et al 2009 Implanted neural electrodes cause chronic, local inflammation that is correlated with local neurodegeneration *J. Neural Eng.* **6** 056003
- [16] Kenneth W H and Gurpreet D 2004 *Neuroprosthetics: Theory and Practice* (Singapore: World Scientific)
- [17] Liu X et al 2006 Evaluation of the stability of intracortical microelectrode arrays *IEEE Trans. Neural Syst. Rehabil. Eng.* **14** 91–100
- [18] McCreery D et al 2010 Neuronal loss due to prolonged controlled-current stimulation with chronically implanted microelectrodes in the cat cerebral cortex *J. Neural Eng.* **7** 036005
- [19] Pikov V et al 2007 Intraspinal stimulation for bladder voiding in cats before and after chronic spinal cord injury *J. Neural Eng.* **4** 356–68
- [20] Mushahwar V K et al 2000 Spinal cord microstimulation generates functional limb movements in chronically implanted cats *Exp. Neurol.* **163** 422–9
- [21] Conrad B P et al 2007 Log-rolling technique producing unacceptable motion during body position changes in patients with traumatic spinal cord injury *J. Neurosurg. Spine* **6** 540–3
- [22] Biran R et al 2007 The brain tissue response to implanted silicon microelectrode arrays is increased when the device is tethered to the skull *J. Biomed. Mater. Res. A* **82** 169–78
- [23] Yang J et al 2007 Electrochemical fabrication of conducting polymer poly(3,4-ethylenedioxythiophene) (PEDOT) nanofibrils on microfabricated neural prosthetic devices *J. Biomater. Sci. Polym. Ed.* **18** 1075–89
- [24] Abdo A et al *In vitro* testing of floating light activated micro-electrical stimulators *Annu. Int. Conf. of the IEEE Engineering in Medicine and Biology Society (Minneapolis, MN, 2009)* pp 626–9
- [25] Lopicque L 1909 Definition experimentale de l'excitabilité C. *R. Acad. Sci.* **67** 280–3
- [26] Elwassif M M et al 2006 Bio-heat transfer model of deep brain stimulation-induced temperature changes *J. Neural Eng.* **3** 306–15
- [27] Abdo A and Sahin M 2011 Feasibility of neural stimulation with floating-light-activated microelectrical stimulators *IEEE Trans. Biomed. Circuits Syst.* **5** 179–88
- [28] Yaroslavsky A N et al 2002 Optical properties of selected native and coagulated human brain tissues *in vitro* in the visible and near infrared spectral range *Phys. Med. Biol.* **47** 2059–73
- [29] Johns M et al 2005 Determination of reduced scattering coefficient of biological tissue from a needle-like probe *Opt. Express* **13** 4828–42
- [30] Johns M 2003 Optical properties of living tissues determined *in vivo* using a thin fiber optic probe *PhD* University of Texas, Arlington
- [31] Kameyama T et al 1996 Morphologic features of the normal human cadaveric spinal cord *Spine (Phila Pa 1976)* **21** 1285–90
- [32] Cogan S F et al 2006 Potential-biased, asymmetric waveforms for charge-injection with activated iridium oxide (AIROF) neural stimulation electrodes *IEEE Trans. Biomed. Eng.* **53** 327–32
- [33] Cui X T and Zhou D D 2007 Poly (3,4-ethylenedioxythiophene) for chronic neural stimulation *IEEE Trans. Neural Syst. Rehabil. Eng.* **15** 502–8
- [34] Gerasimenko Y et al 2008 Epidural stimulation: comparison of the spinal circuits that generate and control locomotion in rats, cats and humans *Exp. Neurol.* **209** 417–25
- [35] Lemay M A et al 2009 Hindlimb endpoint forces predict movement direction evoked by intraspinal microstimulation in cats *IEEE Trans. Neural Syst. Rehabil. Eng.* **17** 379–89
- [36] Moritz C T et al 2007 Forelimb movements and muscle responses evoked by microstimulation of cervical spinal cord in sedated monkeys *J. Neurophysiol.* **97** 110–20
- [37] Henneman E 1980 Organization of the spinal cord and its reflexes *Medical Physiology* **1** 762–86
- [38] McIntyre C C and Grill W M 2002 Extracellular stimulation of central neurons: influence of stimulus waveform and frequency on neuronal output *J. Neurophysiol.* **88** 1592–604
- [39] Ranck J B Jr 1975 Which elements are excited in electrical stimulation of mammalian central nervous system: a review *Brain Res.* **98** 417–40
- [40] Rattay F and Wenger C 2010 Which elements of the mammalian central nervous system are excited by low current stimulation with microelectrodes? *Neuroscience* **170** 399–407
- [41] Stanford J A and Fowler S C 1997 Subchronic effects of clozapine and haloperidol on rats' forelimb force and duration during a press-while-licking task *Psychopharmacology* **130** 249–53
- [42] Barthélemy D et al 2006 Nonlocomotor and locomotor hindlimb responses evoked by electrical microstimulation of the lumbar cord in spinalized cats *J. Neurophysiol.* **96** 3273–92
- [43] Tresch M C and Bizzi E 1999 Responses to spinal microstimulation in the chronically spinalized rat and their relationship to spinal systems activated by low threshold cutaneous stimulation *Exp. Brain Res.* **129** 401–16